

Energy- and k -resolved mapping of the magnetic circular dichroism in threshold photoemission from Co films on Pt(111)

Maximilian Staab,^{1,2} Dmytro Kutnyakhov,¹ Robert Wallauer,¹ Sergey Chernov,¹ Katerina Medjanik,¹ Hans Joachim Elmers,¹ Mathias Kläui,^{1,2} and Gerd Schönhense¹

¹*Institut für Physik, Johannes Gutenberg-Universität Mainz, 55099 Mainz, Germany*

²*Graduate School of Excellence Materials Science in Mainz, Staudinger Weg 9, 55128 Mainz, Germany*

(Received 5 December 2016; published 20 April 2017)

The magnetic circular dichroism in threshold photoemission (TPMCD) for perpendicularly magnetized fcc Co films on Pt(111) has been revisited. A complete mapping of the spectral function $I(E_B, k_x, k_y)$ (binding energy E_B , momentum parallel to surface k_x, k_y) and the corresponding TPMCD asymmetry distribution $A_{\text{MCD}}(E_B, k_x, k_y)$ has been performed for one-photon and two-photon photoemission using time-of-flight momentum microscopy. The experimental results allow distinguishing direct from indirect transitions. The measurements reveal clear band features of direct transitions from bulk bands that show a nontrivial asymmetry pattern. A significant homogeneous background with substantial asymmetry stemming from indirect transitions superposes direct transitions. Two-photon photoemission reveals enhanced emission intensity via an image potential state, acting as intermediate state. The image potential state enhances not only intensity but also asymmetry. The present results demonstrate that two-photon photoemission is a powerful method for mapping the spin-polarized unoccupied band structures and points out pathways for applying TPMCD as a contrast mechanism for various classes of magnetic materials.

DOI: [10.1103/PhysRevB.95.165437](https://doi.org/10.1103/PhysRevB.95.165437)

I. INTRODUCTION

Advanced spin engineering toward next generation magnetic storage and computing devices has become a vivid research field because of the discovery of novel spin phenomena, such as the spin Hall effect [1] and the spin-orbit torque [2]. These spin phenomena are based on the spin-orbit interaction, which can be efficiently investigated by optical excitation [3]. Optical excitation in combination with spin-orbit interaction has been proposed to actively tailor the electron spin, thus leading to the realization of logic operation devices based on fast spin control [4–9]. Finally, for the optical manipulation of the magnetization, the spin-orbit interaction in the unoccupied state is as important as that in the occupied state [10].

A second important task is to explore the physical limits of size and switching times of nanoscopic spin devices, for which one has to develop experimental methods that simultaneously offer high time and spatial resolution. Optical probe pulses can reach the shortest time scales of magnetization dynamics in the femtosecond range. The photoemission signal provides a straightforward combination with spatial resolution. For this purpose, photoemission electron microscopy represents an efficient parallel imaging method providing high spatial resolution superior to optical microscopy [11,12].

Changing the helicity σ of the exciting radiation leads to an asymmetry in the photoelectron yield [13]. X-ray magnetic circular dichroism (XMCD) is one of the most powerful effects to obtain magnetic contrast in photoemission microscopy experiments, as it offers more than 30% asymmetry by exciting spin-orbit split core levels [14–16]. However, the time resolution is limited by the shortest time width of the electron bunches to several picoseconds. Shorter probe pulses for pump-probe experiments are obtained by high-harmonic generators [17] or by femtoslicing methods [18] with, however, limited intensity.

An alternative approach represents threshold photoemission magnetic circular dichroism (TPMCD) for one-photon (1PPE) [19] and two-photon (2PPE) photoemission [20], where electrons are emitted by circularly polarized visible or UV light from ultrafast laser sources with high intensity. TPMCD asymmetries of more than 10% were revealed by using ultraviolet and visible laser light in photoemission from a Ni film on Cu(001) [19,21,22] and for a Co film on Pt(111) [20,23–25].

Although magnetic circular dichroism (MCD) in the x-ray and in the threshold regime is basically caused by the same physical effect, i.e., an interplay of spin-orbit split initial states and exchange split final states, TPMCD is much less understood than XMCD. This is due to the numerous contributing transitions in the case of TPMCD starting from the comparatively small spin-orbit split initial valence bands. In order to apply the TPMCD contrast mechanism for magnetic microscopy and predict the asymmetry values, an in-depth understanding of the origin of the asymmetry is necessary. Previous experimental approaches considered only the total electron yield as observable property.

Here, we investigate the energy and momentum dependence of the TPMCD for the test case of face-centered cubic Co. The comprehensive study of momentum and energy dependence of emitted electrons allows extracting detailed information on the contributing electronic transitions. The valence bands few electron volts below the Fermi level, including spin-orbit coupling and spin-polarization effects, are probed. The experimental results reveal significant asymmetry contributions from direct transitions and photoemission via an image potential state (IPS). The possibility to tune the energetic position of the IPS might provide a pathway to increase the magnetic contrast for various materials taking into account their particular band structure.

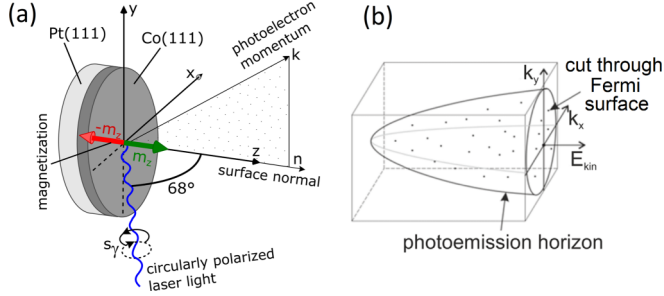


FIG. 1. (a) Geometry of the momentum microscopy measurement yielding the magnetic circular dichroism texture of the full half space. (b) 3D spectral function $I(E_{\text{kin}}, k_x, k_y)$ is limited by the paraboloidic photoemission horizon and by the Fermi level. Adapted from Ref. [26].

II. EXPERIMENTAL

The Pt(111) substrate crystal was prepared in UHV according to the usual standards. Sample transfer between preparation chamber and microscope was performed in UHV. The Co films were deposited using electron beam evaporation. Co films of thickness 4.5 monolayers showed perpendicular magnetic anisotropy in agreement with Ref. [23].

Prior to the transfer into the photoemission chamber the samples were magnetically saturated parallel or antiparallel to the surface normal by a small permanent magnet. For photoelectron excitation we used a Ti:sapphire laser (SpectraPhysics, Type MaiTai) generating pulses of 100-fs duration at a repetition rate of 80 MHz with an average power of 1 W. The laser wavelength is tunable in the range of 750 to 850 nm. Utilizing a frequency doubling BBO crystal wavelengths in the range of 375 to 425 nm can be used. The circular polarization is set by a linear polarizer, followed by a rotatable quarter wave plate. Figure 1 shows the geometry of the experiment. The angle of incidence is 68° , the plane of incidence is the x - z plane. The k -microscope detects all emitted electrons up to the photoemission horizon (i.e., emission parallel to the sample surface). In the k_x, k_y versus E_{kin} plot the data array fills a paraboloid [Fig. 1(b)].

The photoemission intensity is recorded using time-of-flight momentum microscopy. This technique enables a complete mapping of the 3D spectral function $I(E_B, k_x, k_y)$, where E_B is the binding energy, and k_x and k_y are the components of the momentum parallel to the surface and asymmetry $A_{\text{MCD}}(E_B, k_x, k_y)$. The time-of-flight momentum microscope is optimized for imaging of the reciprocal space and it benefits from the maximum parallelization of data acquisition [26]. The distribution of the transversal momentum components is imaged in the back focal plane of the cathode lens. A low-energy drift section serves as energy-dispersive element. For each electron the time of flight is recorded by a time-resolving image detector [27], exploiting the time structure of the femtosecond laser. The time of flight τ is converted into kinetic energy and calibrated at the Fermi edge to obtain the binding energy (for details, see Ref. [12]).

In order to separate the MCD from the nonmagnetic circular dichroism in the angular distribution (CDAD) [28], we acquired four 3D data arrays and calculated the magnetic

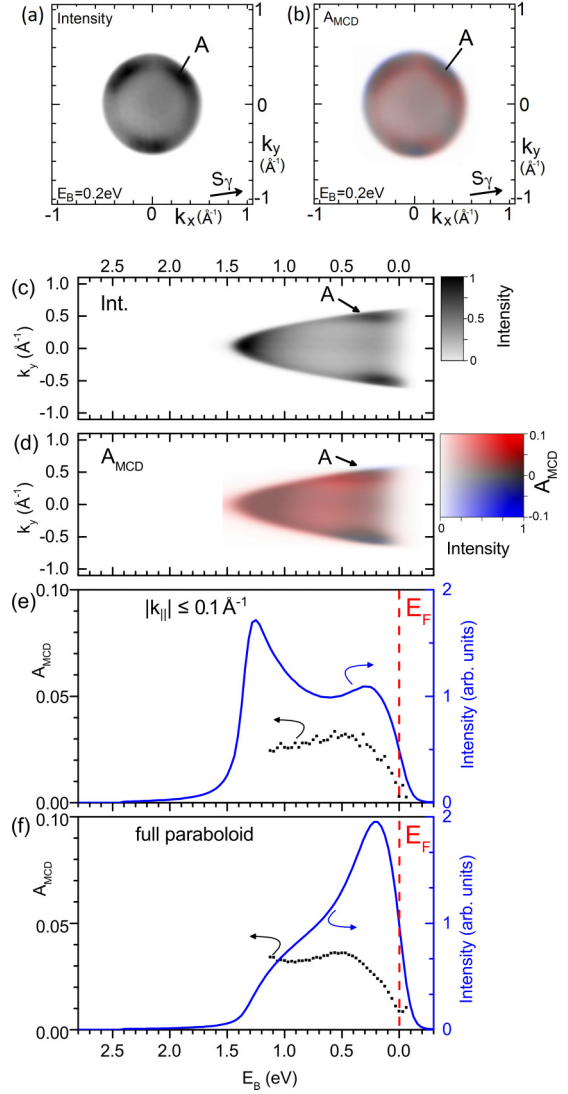


FIG. 2. k -microscopy on clean fcc Co(4.5 ML)/Pt(111) for 2PPE at $2h\nu = 6.2$ eV. The in-plane component of the photon helicity vector S_y is denoted by arrows in (a, b). Intensity (a) and MCD asymmetry (b) k_x - k_y sections for $E_B = 0.2$ eV. Intensity (c) and MCD asymmetry (d) k_y - E sections for $k_x = 0$. Corresponding intensity and MCD asymmetry profiles close to the $\bar{\Gamma}$ point (e) and averaged over the whole paraboloid (f). The gray scale in (c) and the red-gray-blue scale in (d) quantify intensity and MCD asymmetry. \tilde{A}_{MCD} has been determined using Eq. (1).

asymmetry contribution \tilde{A}_{MCD} according to

$$\tilde{A}_{\text{MCD}} = \frac{\sqrt{I_{M\uparrow}^{\sigma+} I_{M\downarrow}^{\sigma-}} - \sqrt{I_{M\downarrow}^{\sigma+} I_{M\uparrow}^{\sigma-}}}{\sqrt{I_{M\uparrow}^{\sigma+} I_{M\downarrow}^{\sigma-}} + \sqrt{I_{M\downarrow}^{\sigma+} I_{M\uparrow}^{\sigma-}}}. \quad (1)$$

III. RESULTS

A. Clean Co/Pt(111)

Figure 2 shows the result of a 2PPE measurement for a Co film of 4.5 monolayers. The photon energy was set to $h\nu = 3.1$ eV. k_x - k_y sections (i.e., the $E = \text{constant}$ momentum discs) of intensity and dichroism asymmetry at $E_B = 0.2$ eV

are shown in Figs. 2(a) and 2(b). Results of the E - k_y section [Figs. 2(c) and 2(d)] reveal the dependence on the binding energy E_B . Figures 2(e) and 2(f) show corresponding intensity and asymmetry profiles in the region within 0.1 \AA^{-1} near $\bar{\Gamma}$ and averaged over all emission angles. Photoemission starts at $E_B = 1.4 \text{ eV}$ reflecting a work function of $\Phi = 4.8 \text{ eV}$ assuming a 2PPE process with $2h\nu = 6.2 \text{ eV}$. Figures 2(a)–2(d) show a band feature (A) with threefold rotation symmetry close to the Fermi level on a relatively homogeneous background. The feature appears at energies of $0 < E_B < 0.5 \text{ eV}$ and a k_{\parallel} value of about 0.5 \AA^{-1} . The symmetry reflects the threefold symmetry of the Γ -L direction. The direction of photon incidence [denoted by the helicity vector S_y in Fig. 2(a)] breaks the threefold symmetry. Band A shows a nonuniform, bipolar MCD asymmetry. The center and integral asymmetry curves in Figs. 2(e) and 2(f) both show a small asymmetry at the Fermi level of only 1%, which increases to a maximum of 3.5% for $E_B = 0.5 \text{ eV}$, followed by a slight drop until 3% at $E_B = 1.2 \text{ eV}$. However, as can be seen in Fig. 2(b), there is a nontrivial asymmetry pattern in the regions of high intensity close to E_F : The ring-type region of positive asymmetry changes into a weak negative asymmetry at the three positions of maximum intensity [see color bar in Fig. 2(d)]. This results in a top-to-bottom sign change of these regions in the $k_x = 0$ section [Fig. 2(d)] and shows up as a drop of the asymmetry curves towards E_F in Figs. 2(e) and 2(f). Close to the bottom of the paraboloid, \tilde{A}_{MCD} may show artifacts due to the large intensity gradient. Therefore, the asymmetry curves in Fig. 2 end at $E_B = 1.3 \text{ eV}$.

B. Cs/Co/Pt(111) at $h\nu = 3.3 \text{ eV}$

In near-threshold photoemission experiments, the accessible momentum and energy range can be increased by evaporating cesium onto the sample surface decreasing the work function. We deposited cesium at very low deposition rates and controlled the work function during data acquisition. Prior to the asymmetry measurements the cesium deposition has been stopped and sufficient idle time ensures a constant work function during acquisition. The photon energy was increased to $h\nu = 3.3 \text{ eV}$ to maximize the accessible binding energy range. The CDAD becomes negligibly small for Cs covered surfaces. Accordingly, MCD results are obtained from data acquired for opposite circularly polarized light.

The results are shown in Fig. 3. The spectral width of 2.5 eV indicates a work function of $\Phi = 4.1 \text{ eV}$. Figures 3(c) and 3(d) reveal a parabolic band B starting at a binding energy of 0.9 eV on a homogeneous background. The parabolic band B represents an IPS acting as an intermediate state that is inherently connected to two-photon photoemission. It does not appear in the case of clean Co because in that case the photon energy is not large enough to reach this state. The MCD asymmetry shown in Figs. 3(e) and 3(f) shows a maximal value of 7% at the Fermi level and decreases to 5% at $E_B = 0.5 \text{ eV}$. The IPS B shows up as a strongly intensified region with the same asymmetry as the background. The previously discussed band feature A close to the Fermi level is superposed by the IPS B (dashed circle) appearing after cesiation. It is eye-catching that for the clean surface the MCD asymmetry

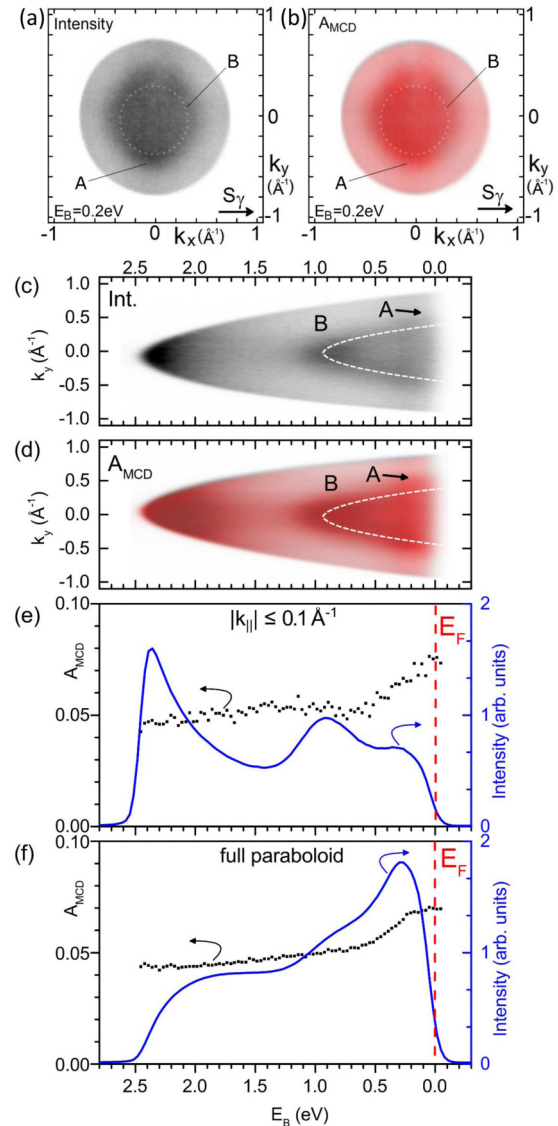


FIG. 3. k -microscopy on cesiated fcc Co(4.5 ML)/Pt(111) ($\Phi = 4.1 \text{ eV}$) for 2PPE at $2h\nu = 6.6 \text{ eV}$. Intensity (a) and MCD asymmetry (b) k_x - k_y sections for $E_B = 0.2 \text{ eV}$. Intensity (c) and MCD asymmetry (d) k_y - E sections for $k_x = 0$. Dashed curves serve to guide the eye. Corresponding intensity and MCD asymmetry curves close to the $\bar{\Gamma}$ point (e) and averaged over the whole paraboloid (f). Color scales, see Fig. 2.

shows a pronounced decrease with decreasing binding energy within a few 100 meV below E_F [Figs. 2(e) and 2(f)], whereas in the cesiated case, A_{MCD} increases in the same binding energy range [Figs. 3(e) and 3(f)].

C. Cs/Co/Pt(111) at $h\nu = 1.65 \text{ eV}$

Increased Cs coverage decreases the work function below 2 eV allowing 2PPE with $h\nu = 1.65 \text{ eV}$. For this case high MCD asymmetries of more than 15% have previously been observed [25]. Figure 4 shows the experimental results for two different work function values. The second measurement has been performed for opposite magnetization direction revealing the reversed asymmetry. The work functions are $\Phi = 2.3 \text{ eV}$ and $\Phi = 2.0 \text{ eV}$. For the lower work function an additional

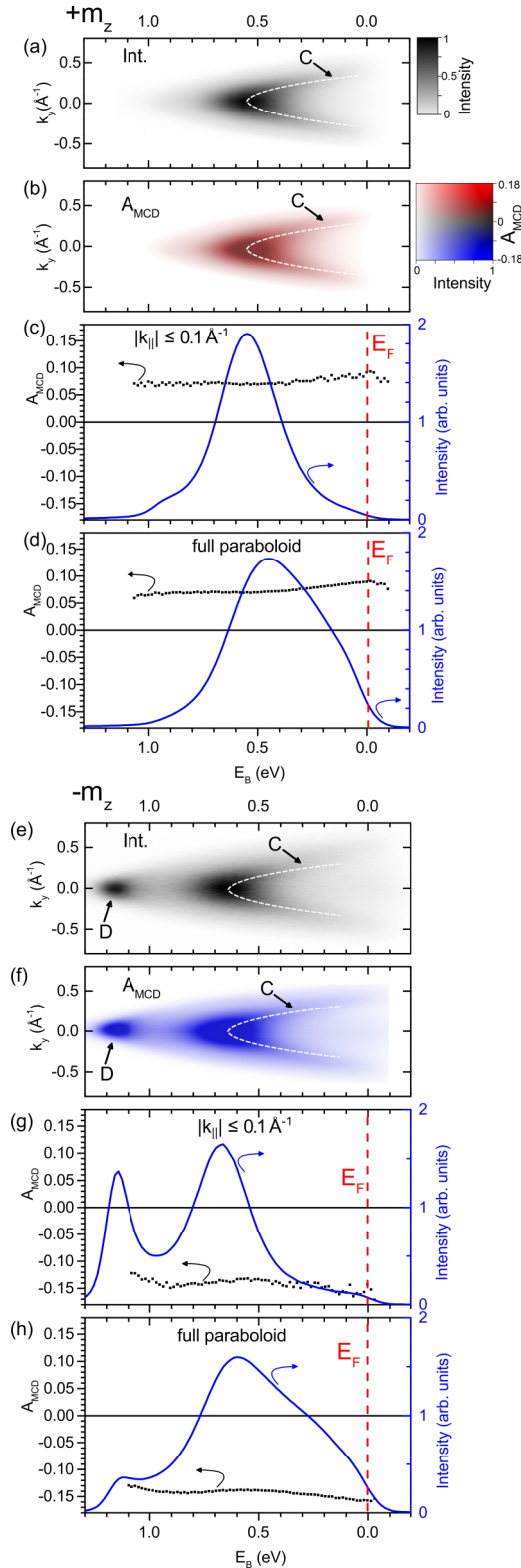


FIG. 4. k -microscopy on cesiated fcc Co(4.5 ML)/Pt(111) for 2PPE at $2h\nu = 3.3$ eV and for $\Phi = 2.3$ eV (a–d) and 2.0 eV (e–h). Intensity (a, e) and MCD asymmetry (b, f) k_y - E sections for $k_x = 0$. Corresponding intensity and MCD asymmetry curves close to the $\bar{\Gamma}$ point (c, g) and averaged over the whole paraboloid (d, h). A_{MCD} has been determined using Eq. (1); color scales, see (b).

intensity maximum appears at the bottom of the paraboloid [Figs. 4(e) and 4(f)].

Both spectra are dominated by the IPS C that exhibits a pronounced intensity maximum at $E_B = 0.55$ eV in Fig. 4(a) and 0.65 eV in Fig. 4(e). The asymmetry curves both show the same qualitative behavior with different sign for m_z and $-m_z$. An additional offset is due to the steadily increasing work function after cesiation caused by the loss of Cs and adsorption of residual gas. Again as for measurements at $h\nu = 3.1$ eV and 3.3 eV (Figs. 2 and 3), the spectra taken at a region close to $\bar{\Gamma}$, and the integral intensity and asymmetries show a similar course. In the case of $\Phi = 2.0$ eV [Figs. 4(e)–4(h)], the maximal asymmetry amounts to 9% at the Fermi level and decreases to about 7% at $E_B = 0.5$ eV and below. In the case of $\Phi = 2.3$ eV the maximal asymmetry is -17% and decreases gradually to about -14% at the bottom of the paraboloid related to an intensity maximum at $E_B = 1.15$ eV (Feature D).

IV. DISCUSSION

The intermediate in the ground-state unoccupied level in two-photon photoemission plays an important role. A prominent feature that one expects to occur for 2PPE is the IPS. Since image potential states are referenced to the vacuum level, changes of the work function also tune the available initial states for IPS-mediated 2PPE processes [29–31].

The energy diagram is sketched in Fig. 5. The bottom of the unoccupied band IPS appears in the photoelectron spectra at ΔE_{IS} . E_1 and ΔE_{IS} are related by the photon energy $h\nu$ and the work function Φ as follows:

$$\Delta E_{\text{IPS}} = E_F + 2h\nu - E_{\text{vac}} + E_1 - h\nu, \quad (2)$$

$$\Leftrightarrow E_1 = \Delta E_{\text{IPS}} + \Phi - h\nu. \quad (3)$$

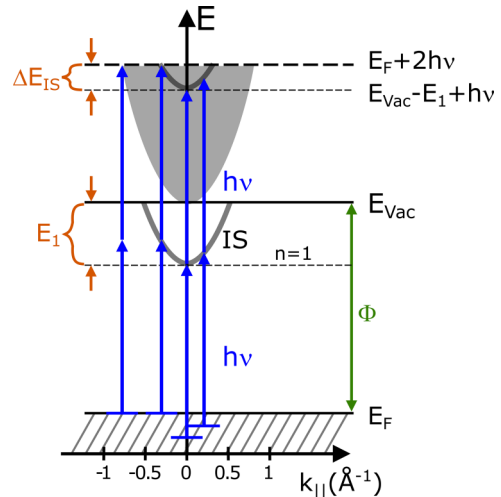


FIG. 5. Energy scheme of a resonant 2PPE transition through an IPS. The bottom of the parabolic band state IS ($n = 1$) is energetically separated from the vacuum level E_{vac} by E_1 . The bottom of the IPS appears in the photoelectron spectra at ΔE_{IS} below the Fermi level E_F . E_1 and ΔE_{IS} are related by the photon energy $h\nu$ and the work function Φ (see text).

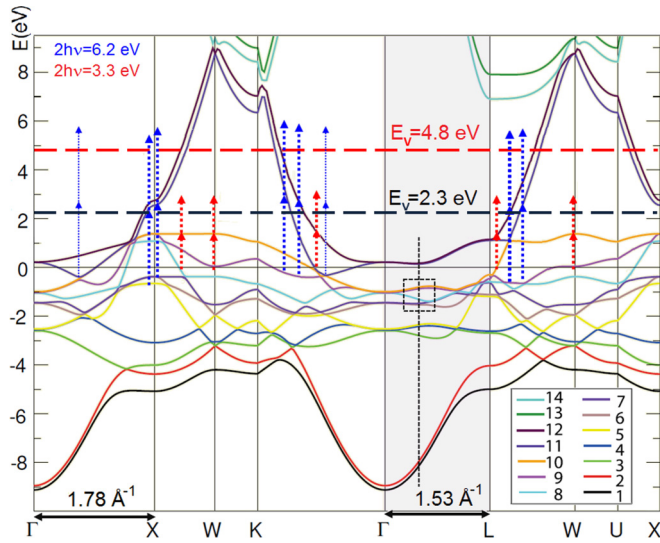


FIG. 6. Calculated band structure of fcc Co taken from Refs. [24,25]. Bands are numbered starting from the lowest energy. Dashed arrows indicate direct transitions into final bulk states. The vertical dashed line denotes the k_z value of $\frac{1}{3}\Gamma\text{L}$.

The IPS observed in our experiment can be distinguished from an occupied surface state by a variation of $h\nu$ or Φ . The IPS shows a parabolic free electron dispersion with parallel momentum because the electrons travel above the surface in a region of negligible lateral potential variations.

For the initial states we consider bulk bands (see Refs. [24,25]), because the MCD asymmetry increases with film thickness [23], indicating rather a bulk behavior of the MCD than a surface induced effect.

Figure 6 shows a band structure calculation for fcc Co (by setting the lattice constant to its bulk value of $a = 0.35457$ nm), which is applicable to the investigated thin-film sample with 4.5-nm thickness. The fcc(111) surface normal points along $\Gamma\text{-L}$.

The MCD asymmetry of a certain photo excitation channel is supposed to be highly dependent on the presence of a stationary intermediate state in the first excitation step (for 2PPE processes) or a final state (for 1PPE processes) [25]. In the conventional model of photoemission, the electronic transitions obey the condition that k_{\parallel} stays constant. Such transitions are referred to as “direct transitions” [32]. Excitations into evanescent states, which are strongly damped final surface states, cannot explain the bulk sensitivity of the MCD effect which has been reported in Ref. [23]. In threshold photoemission there is only little excess energy that can go into parallel momentum. The refraction of the photoelectron wave at the surface barrier is described by

$$k_{\parallel} = \sin \Theta_{\text{out}} \sqrt{\frac{2m}{\hbar^2} E_{\text{kin}}} = \sin \Theta_{\text{in}} \sqrt{\frac{2m}{\hbar^2} (E_{\text{kin}} + V_0)}, \quad (4)$$

where m is the mass of the electron, \hbar is the reduced Planck constant, and V_0 is the inner potential (for the present case of Co we have $V_0 = 15$ eV). The emission angle Θ increases upon transmission through the surface [32]. Hence, although above the surface there is emission into the full half space, the internal emission angle Θ_{in} is strongly reduced. For the

range of kinetic energies of 1 to 3 eV we find for the electrons close to the Fermi level maximum internal emission angles of $\Theta_{\text{in}} = 14.5^\circ$ to 24.1° . Equation (4) thus translates the full half space on the vacuum side into a quite narrow internal solid angle interval (termed “escape cone”) [32]. Consequently, photoemitted electrons are expected to originate from direct transitions close to the $\Gamma\text{-L}$ direction.

However, the direct transition model cannot describe near-threshold photoemission for the following reason: The zero of kinetic energy and hence the bottom of the free-electron-like parabolic final state band is given by the inner potential V_0 . Since photon momentum can be neglected in near-threshold photoemission, we obtain for the perpendicular momentum component:

$$k_{\perp} = \sqrt{\frac{2m}{\hbar^2} (nh\nu - \Phi + V_0)}, \quad (5)$$

where n is the number of photons $h\nu$ involved in the transition and Φ is the work function. The final state momentum is thus related to a certain k coordinate in the Brillouin zone. The relevant reciprocal lattice vector along the fcc(111) direction (perpendicular to the surface) is $G_{111} = 1.53 \text{ \AA}^{-1}$. For an excess energy between 1 and 3 eV we obtain k_{\perp} values between $1.33 G_{111}$ and $1.41 G_{111}$. It means that momentum conservation can only be fulfilled if a reciprocal lattice vector G_{111} is involved. The essential point is that there is no branch of this parabola that fits to a direct transition, i.e., energy and momentum conservation cannot be fulfilled simultaneously.

Since the common model of photoemission cannot explain near-threshold photoemission, Refs. [24,25] proposed a different mechanism. Spin-selective interband-excitations along many other crystallographic directions may contribute to photoemission intensity via nondirect transitions involving electron scattering events. Possible direct transitions (for $2h\nu = 6.6$ eV) are shown as dashed blue arrows in Fig. 6. They appear in high-symmetry directions $\Gamma\text{-K}$, L-W , and $\Gamma\text{-X}$, but also in a multitude of arbitrary directions. The hypothesis is that the electrons in these spin-polarized states are scattered such that they can escape from the surface. This is mediated by the broken translational symmetry at the surface which may lift k -conservation. Electronic states with parallel momentum along $\Gamma\text{-X}$, in particular, allow for a resonant transition with high dichroism and spin asymmetry.

Whereas in photocurrent measurements the total electron yield and consequently an averaged asymmetry is measured, the present experiment resolves the final-state energy. Thus, we selectively detect the contributions of the different binding energies. Increasing photon energy adds more photoelectrons to the total yield, which contribute to the total asymmetry. Our experiment shows that states at larger binding energies with small density of states and photoemission intensity, respectively, can cause a large MCD signal, e.g., as in Fig. 4(g). The data shows that most of the intensity originates from the IPS C and the bottom of the parabola D, whereas the asymmetry is equally high in the regions of low intensity between C and D. The asymmetry spectra of Figs. 2(d) and 2(f) reveal that the asymmetry is slightly decreasing with increasing binding energy, starting at $E_B = 0.5$ eV. This is in good agreement with Ref. [25], since at lower photon

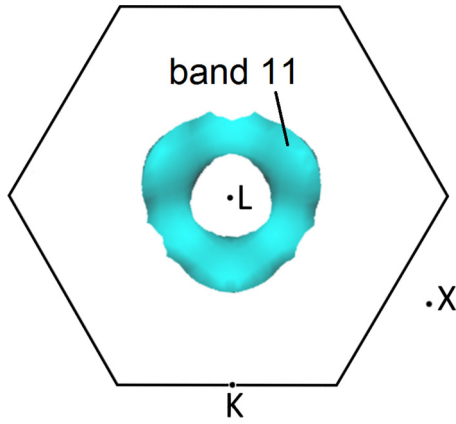


FIG. 7. Projection of a section of Γ to $\frac{1}{3}\Gamma L$ of the fcc Co minority Fermi surface. This representation contains the symmetry points L, K, X. The turquoise feature originates from band 11 and shows a threefold symmetry. From [33].

energies, electrons with larger binding energies get excluded from the integral photoemission yield. Two more features can be observed in Fig. 2: First, there is a high intensity close to the Fermi level, which shows a threefold symmetry in the k_x - k_y section and creates a bipolar MCD asymmetry pattern. This feature indicates a band that is located in the Γ -X or Γ -K direction. Assuming the accessible photoemission horizon, the corresponding band can be identified as the minority band 11 (cf. Fig. 6). The corresponding transitions are shown as thin dashed blue arrows. Since there is no stationary intermediate state included, based on existing theory, there is no indication for a contribution to the MCD asymmetry. However, in the asymmetry spectra there is a change in the sign of the MCD asymmetry inside this threefold feature. Subsequently, the integral asymmetry curve exhibits a pronounced drop at the corresponding binding energies E_B .

In the surface projection of the volume band structure calculation (Fig. 6), the k values that correspond to feature A convert into $k_{\parallel} = 0.53 \text{ \AA}^{-1}$ in case of the Γ -X direction and $k_{\parallel} = 0.54 \text{ \AA}^{-1}$ in case of the Γ -K direction. Figure 7 illustrates a cut through the fcc Co minority Fermi surface at $k_z = \frac{1}{3}\Gamma L$ that resembles the excitation with $2h\nu = 6.2 \text{ eV}$. The location of the turquoise feature in Fig. 7 corresponds to the minority band 11 in Fig. 6. Its threefold symmetry agrees with the experimentally observed feature A in Fig. 2 and confirms the fcc structure.

Second, we see a homogeneous background, which indicates contributing transitions along a manifold of directions. Since the direct escape from the surface is forbidden except for a cone around Γ -L, there must be electron-phonon or electron-magnon scattering processes involved. The scattering process causes a loss of the information on the k value of the electron in its initial state. Additionally, it has been shown recently [34] that for highly correlated materials such as d -band ferromagnets like Co, the assumption of distinct sharp bands is not strictly valid. Instead, electron-electron correlation results in a smearing of the bands in the region of $0 < E_B < 5 \text{ eV}$. This is different to metals without strongly correlated electrons, which show much sharper bands close to the Fermi

level; a prototype example is tungsten [35]. However, the influence of transitions along crystallographic directions other than Γ -L is also evident from the high MCD of the background signal.

As seen in the comparison of Figs. 2 and 3, the deposition of cesium onto the surface does not only lower the work function of the surface, but it also considerably changes the photoemission pattern. The IPS is dominating the spectral distribution in Fig. 3. Variation of photon energy and/or work function influences the energetic position of band B, which confirms that it originates from a resonant transition trough an IPS.

The present energy and k -resolved results clearly show that the IPS determines the main part of the emitted intensity. The IPS enables direct transitions along the Γ -L direction, at least for the first excitation step. The observed photoemission intensity is a convolution of the parabolic IPS with the initial state. Near $k_z = \frac{1}{3}\Gamma L$ a flat band (square in Fig. 6) occurs with a correspondingly high density of states. This leads to the enhanced intensity near $\bar{\Gamma}$ and at $E_B = 0.65 \text{ eV}$ in Fig. 4 for $2h\nu = 3.3 \text{ eV}$. The same flat band might also be responsible for the enhanced intensity at $E_B = 1 \text{ eV}$ in Fig. 3 for $2h\nu = 6.6 \text{ eV}$. The high intensity in Fig. 3 at $E_B = 2.3 \text{ eV}$ could be caused by the lower-lying band near $k_z = \frac{1}{3}\Gamma L$ (see Fig. 6). Our earlier work [25] could not detect any k - or E_B -dependence, hence the presence of the emission channel via the IPS was not recognized.

Since the additional photoemission intensity caused by the IPS reveals an almost similar MCD asymmetry as the background intensity it does not show up as a pronounced feature in the asymmetry spectra and can thus be easily overlooked in k -integrated measurements. As shown in Fig. 8, the IPS selects particular bands for the photoemission process. The work function Φ as well as the photon energy directly tune the accessibility of the corresponding initial states. If the IPS “hits” a region of E_B that possesses a high density of states, there is an enhanced intensity in the photoemission spectra. Since initial states have a certain spin polarization and a majority or minority character, respectively, it is possible to directly impact the integrally measured MCD asymmetry.

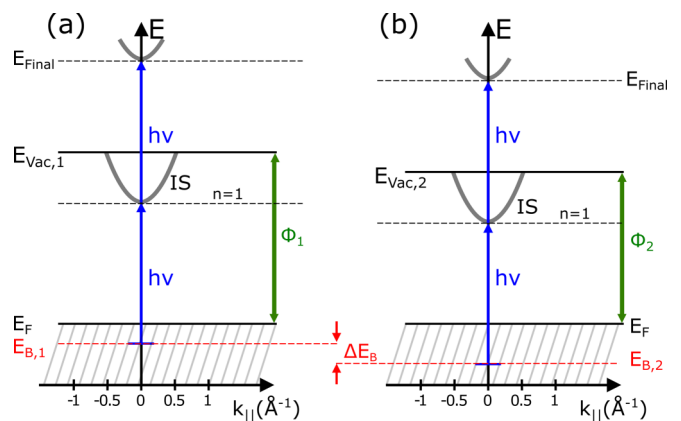


FIG. 8. The IPS selects particular initial bands for the photoemission process. The energetic position of the band $E_{B,1,2}$ is defined by the work function $\Phi_{1,2}$ (as shown in a and b) and the photon energy $h\nu$.

Please note that there is a source of error in the overall measured intensities that may result in an offset of the calculated MCD asymmetries. These changes of intensity may partly be caused by artifacts: The change of the helicity can slightly affect the intensity of the incident light and a change of the analyzed region of interest on the sample after magnetization and sample transfer might change the photoemission yield. The strongest contribution is caused by the cesiation procedure itself. Cesium coverage of metals was shown to be a nontrivial measure as it for instance changes with time [36].

V. CONCLUSION

We investigated the spectroscopic signatures in perpendicularly magnetized ultrathin Co/Pt(111) films. A general understanding of MCD originating from a combination of exchange splitting and spin-orbit coupling has been given in Ref. [37]. However, there is only little knowledge on the microscopic and material-specific origin of this effect. Previous investigations focused on measurements of the total photoemission yield [24,25].

These results suggested a predominant contribution from indirect photoemission transitions involving inelastic electron scattering events. In the particular case of Co(111) there are no direct transitions possible in the vicinity of the photoemission threshold because energy and momentum conservation cannot be fulfilled simultaneously. The fact that the free-electron-like final state band has no branch close to the vacuum level and at low parallel momentum is typical for many materials. Along this argumentation, Hild *et al.* [24,25] proposed a mechanism for 2PPE where the circular dichroism of the total photoelectron yield is governed by direct transitions along directions other than the perpendicular emission direction Γ -L.

We performed a comprehensive measurement of the full spectral distribution $I(E_B, k_x, k_y)$ of photoelectrons along with the MCD asymmetry distribution $A_{\text{MCD}}(E_B, k_x, k_y)$. We utilized the fundamental ($h\nu = 1.55$ eV) and the second harmonic ($h\nu = 3.1$ eV) of a femtosecond Ti:sapphire laser. The 2PPE photoemission patterns of the clean sample (Fig. 2),

when excited by the second harmonic, show a pronounced band feature with threefold symmetry and a bipolar MCD signature that indicates the contribution of majority and minority bands. We tentatively attribute this feature to a band that has a minimum at $k_{\parallel} = 0.53 \text{ \AA}^{-1}$ in case of the Γ -X direction and $k_{\parallel} = 0.54 \text{ \AA}^{-1}$ in case of the Γ -K direction (thin arrow in Fig. 6, left panel). This is illustrated in the $k_z = \frac{1}{3}\Gamma\text{L}$ projection of the calculated band structure shown in Fig. 7. The background shows a rather homogenous intensity and dichroism asymmetry, but without having a clearly visible k -dependence. Lowering the work function by cesium deposition (Fig. 3) results in a strongly enhanced two photon photoemission intensity which is due to resonant 2PPE transitions via an IPS. Dichroism measurements using the fundamental of the laser (Fig. 4) showed relatively constant MCD asymmetries of more than 15%, which is in good agreement with Ref. [25]. The homogeneous background intensity and MCD asymmetry confirm the strong contribution of direct transitions along crystallographic directions other than Γ -L.

However, the analysis of $I(E_B, k_x, k_y)$ reveals that there is a considerable contribution originating from an IPS serving as an intermediate state for the 2PPE photoemission process, which is not visible in total yield measurements. The IPS provides a resonant 2PPE channel and therefore intensifies the emission from certain initial states in the occupied part of the valence band. These findings show that intermediate states (here an IPS) as well as initial band states dominantly contribute to the observed asymmetry. In contrast, for the clean surface at $h\nu = 3.1$ eV these two contributions are missing for energetic reasons. Hence, a relatively large background intensity dominates the emission intensity.

ACKNOWLEDGMENTS

M.S. is a recipient of a DFG fellowship through the Excellence Initiative by the Graduate School Materials Science in Mainz (Grant No. GSC266). The project is funded by the DFG through the SFB/TR173 Spin+X.

-
- [1] Y. K. Kato, R. C. Myers, A. C. Gossard, and D. D. Awschalom, *Science* **306**, 1910 (2004).
 - [2] D. Ralph and M. Stiles, *J. Magn. Magn. Mater.* **320**, 1190 (2008).
 - [3] H. Ebert, *Rep. Prog. Phys.* **59**, 1665 (1996).
 - [4] D. Hsieh, Y. Xia, D. Qian, L. Wray, J. H. Dil, F. Meier, J. Osterwalder, L. Patthey, J. G. Checkelsky, N. P. Ong, A. V. Fedorov, H. Lin, A. Bansil, D. Grauer, Y. S. Hor, R. J. Cava, and M. Z. Hasan, *Nature* **460**, 1101 (2009).
 - [5] J. W. McIver, D. Hsieh, H. Steinberg, P. Jarillo-Herrero, and N. Gedik, *Nat. Nanotechnol.* **7**, 96 (2012).
 - [6] C. Jozwiak, C.-H. Park, K. Gotlieb, C. Hwang, D.-H. Lee, S. G. Louie, J. D. Denlinger, C. R. Rotundu, R. J. Birgeneau, Z. Hussain, and A. Lanzara, *Nat. Phys.* **9**, 293 (2013).
 - [7] A. Junck, G. Refael, and F. von Oppen, *Phys. Rev. B* **88**, 075144 (2013).
 - [8] J. Sanchez-Barriga, A. Varykhalov, J. Braun, S.-Y. Xu, N. Alidoust, O. Kornilov, J. Minar, K. Hummer, G. Springholz, G. Bauer, R. Schumann, L. V. Yashina, H. Ebert, M. Z. Hasan, and O. Rader, *Phys. Rev. X* **4**, 011046 (2014).
 - [9] C. Kastl, C. Karnetzky, H. Karl, and A. W. Holleitner, *Nat. Commun.* **6**, 6617 (2015).
 - [10] T. Nakazawa, N. Takagi, Maki Kawai, H. Ishida, and R. Arafune, *Phys. Rev. B* **94**, 115412 (2016).
 - [11] G.-K.-L. Marx, H. J. Elmers, and G. Schönense, *Phys. Rev. Lett.* **84**, 5888 (2000).
 - [12] G. Schönense, K. Medjanik, and H. Elmers, *J. Electron, Spectrosc. Relat. Phenom.* **200**, 94 (2015).
 - [13] G. Schütz, W. Wagner, W. Wilhelm, P. Kienle, R. Zeller, R. Frahm, and G. Materlik, *Phys. Rev. Lett.* **58**, 737 (1987).
 - [14] B. T. Thole, P. Carra, F. Sette, and G. van der Laan, *Phys. Rev. Lett.* **68**, 1943 (1992).

- [15] P. Carra, B. T. Thole, M. Altarelli, and X. Wang, *Phys. Rev. Lett.* **70**, 694 (1993).
- [16] J. Stöhr, *J. Magn. Magn. Mater.* **200**, 470 (1999).
- [17] C. La-O-Vorakiat, M. Siemens, M. M. Murnane, H. C. Kapteyn, S. Mathias, M. Aeschlimann, P. Grychtol, R. Adam, C. M. Schneider, J. M. Shaw, H. Nembach, and T. J. Silva, *Phys. Rev. Lett.* **103**, 257402 (2009).
- [18] K. Holldack, J. Bahrtdt, A. Balzer, U. Bovensiepen, M. Brzhezinskaya, A. Erko, A. Eschenlohr, R. Follath, A. Firsov, W. Frentrup, L. Le Guyader, T. Kachel, P. Kuske, R. Mitzner, R. Muller, N. Pontius, T. Quast, I. Radu, J.-S. Schmidt, C. Schüssler-Langeheine, M. Sperling, C. Stamm, C. Trabant, and A. Fohlisch, *J. Synchrotron Radiat.* **21**, 1090 (2014).
- [19] T. Nakagawa and T. Yokoyama, *Phys. Rev. Lett.* **96**, 237402 (2006).
- [20] K. Hild, J. Maul, G. Schönhense, H. J. Elmers, M. Amft, and P. M. Oppeneer, *Phys. Rev. Lett.* **102**, 057207 (2009).
- [21] T. Nakagawa, I. Yamamoto, Y. Takagi, K. Watanabe, Y. Matsumoto, and T. Yokoyama, *Phys. Rev. B* **79**, 172404 (2009).
- [22] M. Kronseder, J. Minar, J. Braun, S. Günther, G. Woltersdorf, H. Ebert, and C. H. Back, *Phys. Rev. B* **83**, 132404 (2011).
- [23] K. Hild, J. Emmel, G. Schönhense, and H. J. Elmers, *Phys. Rev. B* **80**, 224426 (2009).
- [24] K. Hild, G. Schönhense, H. J. Elmers, T. Nakagawa, T. Yokoyama, K. Tarafder, and P. M. Oppeneer, *Phys. Rev. B* **82**, 195430 (2010).
- [25] K. Hild, G. Schönhense, H. J. Elmers, T. Nakagawa, T. Yokoyama, K. Tarafder, and P. M. Oppeneer, *Phys. Rev. B* **85**, 014426 (2012).
- [26] S. V. Chernov, K. Medjanik, C. Tusche, D. Kutnyakhov, S. A. Nepijko, A. Oelsner, J. Braun, J. Minar, S. Borek, H. Ebert, H. J. Elmers, J. Kirschner, and G. Schönhense, *Ultramicroscopy* **159**, 453 (2015).
- [27] A. Oelsner, O. Schmidt, M. Schicketanz, M. Klais, G. Schönhense, V. Mergel, O. Jagutzki, and H. Schmidt-Böcking, *Rev. Sci. Instrum.* **72**, 3968 (2001).
- [28] G. Schönhense, *Phys. Scr.* **T31**, 255 (1990).
- [29] Edited by T. Fauster, W. Steinmann, and P. Halevi, *Electromagnetic Waves: Recent Developments in Research* (Elsevier, Amsterdam, 1994).
- [30] U. Höfer, I. L. Shumay, C. Reuss, U. Thomann, W. Wallauer, and T. Fauster, *Science* **277**, 1480 (1997).
- [31] O. Andreyev, Y. M. Koroteev, M. Sánchez Albaneda, M. Cinchetti, G. Bihlmayer, E. V. Chulkov, J. Lange, F. Steeb, M. Bauer, P. M. Echenique, S. Blügel, and M. Aeschlimann, *Phys. Rev. B* **74**, 195416 (2006).
- [32] S. Hüfner, *Photoelectron Spectroscopy* (Springer, Berlin, 1995).
- [33] T.-S. Choy, J. Naset, J. Chen, S. Hershfield and C. Stanton, *Bulletin of the American Physical Society* **45**, L36 42 (2000).
- [34] A. Grechnev, I. Di Marco, M. I. Katsnelson, A. I. Lichtenstein, J. Wills, and O. Eriksson, *Phys. Rev. B* **76**, 035107 (2007).
- [35] K. Miyamoto, A. Kimura, K. Kuroda, T. Okuda, K. Shimada, H. Namatame, M. Taniguchi, and M. Donath, *Phys. Rev. Lett.* **108**, 066808 (2012).
- [36] L. W. Swanson and R. W. Strayer, *J. Chem. Phys.* **48**, 2421 (1968).
- [37] W. Kuch and C. M. Schneider, *Rep. Prog. Phys.* **64**, 147 (2000).